

Microwave nanobolometer based on proximity Josephson junctions

J. Govenius,^{1,*} R. E. Lake,¹ K. Y. Tan,¹ V. Pietilä,¹ J. K. Julin,² I. J. Maasilta,² P. Virtanen,³ and M. Möttönen^{1,3}

¹*QCD Labs, COMP Centre of Excellence, Department of Applied Physics,
Aalto University, P.O. Box 13500, FIN-00076 Aalto, Finland*

²*Nanoscience Center, Department of Physics, P.O. Box 35, FIN-40014 University of Jyväskylä, Finland*

³*O. V. Lounasmaa Laboratory, Aalto University, P.O. Box 15100, FIN-00076 Aalto, Finland*

(Dated: August 3, 2018)

We introduce a microwave bolometer aimed at high-quantum-efficiency detection of wave packet energy within the framework of circuit quantum electrodynamics, the ultimate goal being single microwave photon detection. We measure the differential thermal conductance between the detector and its heat bath, obtaining values as low as 5 fW/K at 50 mK. This is one tenth of the thermal conductance quantum and corresponds to a theoretical lower bound on noise-equivalent-power of order 10^{-20} W/ $\sqrt{\text{Hz}}$ at 50 mK. By measuring the differential thermal conductance of the same bolometer design in substantially different environments and materials, we determine that electron-photon coupling dominates the thermalization of our nanobolometer.

I. INTRODUCTION

Reaching noise-equivalent-power (NEP) of 10^{-20} W/ $\sqrt{\text{Hz}}$ in radiation sensors is an important goal for space-based telescope because it allows cosmic background radiation limited spectroscopy in the THz regime.^{1,2} What intrigues us however, is that such low noise levels would also enable direct measurement of wave packet energy in circuit quantum electrodynamics (cQED).^{3,4} For example, NEP of 10^{-21} W/ $\sqrt{\text{Hz}}$ allows resolving an individual 10 GHz microwave photon emitted from a qubit or resonator with energy relaxation time of 10 μs . Even a more modest NEP of 10^{-18} W/ $\sqrt{\text{Hz}}$ enables on-chip phase-insensitive energy measurements of multi-photon wave packets, such as dispersive qubit measurement pulses.^{3,5} Since the energy of a wave packet and the voltage produced by it correspond to non-commuting quantum-mechanical observables, such single-shot energy measurements are fundamentally limited in precision when using traditional microwave amplifiers which amplify voltage.⁶ The difference between these measurement schemes is crucial in single-shot measurements of non-classical pulses containing a definite amount of energy, such as in the Hong-Ou-Mandel effect or in linear optics quantum computation.^{7,8} Although the Hong-Ou-Mandel effect can be verified by ensemble averaging traditional voltage measurements,^{9,10} that approach is not scalable to more complex experiments that require feedback conditioned on energy measurements. In addition to low NEP, such feedback experiments require high bandwidth as well as absorption and detection of nearly all of the incident microwave radiation, i.e., high quantum efficiency. On the other hand, bolometry in cQED does not require a broad dynamic range or antenna coupling to off-chip radiation sources.

Transition edge sensors^{1,11–15} (TES) and kinetic inductance detectors^{16–18} are the most mature low-temperature bolometer technologies. Use of other superconductor weak links,^{19–22} semiconductor nanostructures,^{23–25} graphene,^{26–29} carbon nanotubes,³⁰ and quantum capacitance^{31–33} has also been experimentally explored. State-of-the-art nanoscale TESs,¹² semiconducting detectors,²⁵ and quantum capacitance detectors³³ have reached phenomenal NEP at THz frequencies but their quantum efficiency relies on high-

energy input photons compared to a device-specific energy scale, e.g., the minimum energy for breaking Cooper pairs in a quantum capacitance detector or the energy above which the TES impedance is well approximated by its normal-state resistance.³⁴ Furthermore, TESs and semiconducting detectors are typically read out using low-bandwidth amplifiers.^{11,12,25} Our hot-electron³⁵ nanobolometer addresses the low-frequency impedance matching issue by including a nanoscale resistive absorber element that is thermally strongly coupled to the thermometer element, but in a configuration that allows independent electrical design and operation of the two elements. This allows absorbing all incoming radiation down to arbitrarily low frequency by matching the resistance of the absorber element to the characteristic impedance of the input transmission line, typically 50 Ω in cQED. The thermometer element on the other hand is mostly reactive, enabling the use of a fast rf-coupled readout technique similar to quantum capacitance detectors. Probing changes in a reactive rather than a resistive thermometer allows the use of a larger readout power for a given maximum tolerable level of measurement-induced heating. This is important for minimizing the effect of noise added by the rest of the amplification and digitization circuitry and hence for approaching the theoretical limits on NEP. We also note that our detector demonstrates experimentally the temperature to inductance transduction mechanism proposed in the so called Josephson proximity sensor.^{36,37}

We report on measurements of thermal conductance between our nanobolometer and its heat bath. This is an important first step toward demonstrating feasibility of our design since thermal conductance G is an essential parameter in determining the magnitude of thermal energy fluctuations between the bolometer and its heat bath. These fluctuations set a lower bound on NEP because temperature measurements cannot distinguish them from variations in input signal power.^{38–40} Generally, fluctuations of order $\sqrt{(GT)(k_B T)}$ arise from shot noise intrinsic to any Poisson process that transports an average power GT in packets of typical size $k_B T$, but the exact expression depends on details of the thermalization and thermoelectric feedback mechanisms.³⁸ We find that for our rf coupled sensors the differential thermal

conductance is 5 fW/K at 50 mK. This implies that the theoretical lower bound on NEP set by thermal energy fluctuations is of order 10^{-20} W/ $\sqrt{\text{Hz}}$. We note that similar thermal conductances have been previously achieved in suspended TESs¹³ and even lower values in a hot-electron TES,¹¹ but without impedance matching at microwave input frequencies and with substantially lower readout bandwidth.

By measuring the same bolometer design in different electromagnetic environments and by using different materials, we find that the dominant heat link between our sensor and the environment is the electron–photon thermal conductance. Like other single-mode conduction channels, the electron–photon conductance is bound from above by the universal quantum of thermal conductance^{41–45} $G_Q = \pi^2 k_B^2 T / 3h$, which is reached when the detector and environment impedances are matched at thermal excitation frequencies.⁴⁶ By engineering the electromagnetic environment in the vicinity of the sensor, we reduce the total differential thermal conductance to one tenth of G_Q at 50 mK, i.e., 5 fW/K. This value is likely dominated by parasitic electromagnetic coupling to the environment.

II. PRINCIPLE OF OPERATION

The central component of our nanobolometer is a diffusive normal-metal nanowire contacted by three superconductor leads, which together form two diffusive superconductor–normal-metal–superconductor (SNS) junctions with a total normal-metal volume of order $(100 \text{ nm})^3$ [see Fig. 1(b) and Table I]. We fabricated all nanowires with electron beam lithography using shadow angle evaporation of $\text{Au}_x\text{Pd}_{1-x}$ as normal metal and Al or Nb as superconductor on oxidized silicon substrates. We estimate $x \approx 0.75$ based on evaporation parameters and known alloy stabilities.⁴⁷ Electrical measurements were performed in a cryostat with base temperature of 10 mK. At a bath temperature of 100 mK, the long junction is an ohmic resistor $R_{N,\text{long}}$ in all samples, while the short junction supports a non-dissipative supercurrent with clear switching and retrapping at currents of order 100 nA. Even at 10 mK, the long junction shows a mere reduced resistance at the smallest currents (< 10 nA) but no switching. This allows us to neglect the reactive component of the long junction admittance.

Samples A, B, C, and N were dc coupled and measured using sub-kHz frequencies [dc mode, Fig. 1(c)], while Samples R and F were capacitively coupled and measured at microwave frequencies [rf mode, Fig. 1(d)]. Shunting lead G [Fig. 1(b)] to ground through a small resistance in dc mode and by a large capacitor (C_1) in rf mode prevents electrical cross-talk between the long and short junctions during device operation, but does not prevent thermalization^{48,49} between the junctions on relevant timescales. Therefore, a single temperature T_e accurately describes the electronic system of the entire normal-metal nanowire. In all samples, the long junction heats the electron gas (P_{local}) while the short junction transduces T_e into an electrical signal. In dc mode, a fixed current bias heats the electrons with $P_{\text{local}} =$

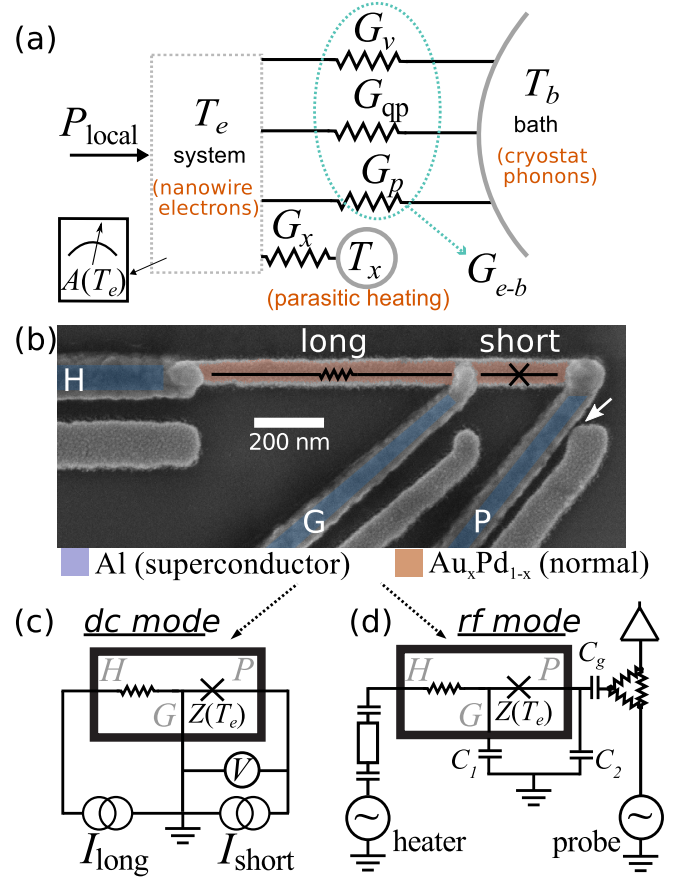


FIG. 1. (Color online) (a) Thermal model of the electron system at temperature T_e coupled to a bath at T_b through photonic (G_v), quasiparticle (G_{qp}), and phononic (G_p) thermal conductances that comprise the total conductance (G_{e-b}). Here, G_x quantifies coupling to a parasitic bath (T_x), P_{local} is local heating power, and $A(T_e)$ is a temperature-dependent observable. (b) Micrograph of Sample A. The normal-metal nanowire is contacted by three superconductor leads: heater (H), ground (G) and temperature probe (P). The white arrow indicates an unintentional galvanic contact present only in Sample A. (c) Simplified electrical schematic for measurement of the temperature-dependent sensor impedance $Z(T_e)$ in Samples A, B, C, and N (dc mode). (d) Same as (c) but for Samples R and F (rf mode).

$I_{\text{long}}^2 R_{N,\text{long}}$, while the current at which the short junction switches from the superconducting state to the normal state indicates electron temperature, a technique known as proximity-effect thermometry.^{50–52} In rf mode, a transmission line delivers P_{local} at several GHz, while a small amplitude excitation at hundreds of MHz probes the T_e dependent inductance of the short junction.

A. dc mode

In dc mode, we ramp the current bias through the short junction $I_{\text{short}}(t)$ linearly over several milliseconds while measuring voltage V over it in a four-wire configuration. As the

short SNS junction switches from the superconducting state to the normal state, V jumps from zero to $I_{\text{short}} R_{N,\text{short}}$ at a stochastic time t_{switch} . Since the ramp is much slower than the inverse bandwidth of our electrical lines, we can convert t_{switch} directly to a current $I_{\text{short}}(t_{\text{switch}})$. We repeat this I_{short} bias cycle approximately 10^3 times and record a histogram of switching currents [Fig. 2(a)] as well as the voltage trace averaged over all repetitions. We then define either the median of the switching current distribution or the current at which V on average crosses $0.5 \times I_{\text{short}} R_{N,\text{short}}$ as a typical switching current I_s^* . This I_s^* defines an uncalibrated electron temperature probe $A(T_e)$ [Fig. 1(a)] in dc mode. We call it uncalibrated because we do not attempt to deduce the absolute temperature T_e or the theoretical critical current I_c from $A(T_e)$. Note also that the heating current $I_{\text{long}} \ll I_s^*$.

A key assumption in our model is that I_s^* does not vary with T_b at constant T_e . Mathematically, we ignore $|\partial_{T_b} I_s^*(T_e, T_b)|$ as negligible compared to $|\partial_{T_e} I_s^*|$ within the temperature range of interest. Physically, we assume that phase fluctuations across the junction are damped by the electron gas at T_e , rather than the external environment at T_b . This is reasonable for SNS junctions given their high plasma frequency and strong dissipation at high frequencies.⁵³ Furthermore, the similarity of switching current distributions along contours of I_s^* [see Fig. 2(a)] supports the validity of the assumption; it suggests that the distributions are well described by a single parameter, which would be surprising if $|\partial_{T_b} I_s^*| \sim |\partial_{T_e} I_s^*|$. Also note that overdamped electrical response at high frequencies is not contradictory with the observed hysteretic switching and retrapping behavior which can arise due to Joule heating.⁵⁴

B. rf mode

For Sample R (F), the long junction absorbs P_{local} from a monochromatic 8.8 GHz (6.74 GHz) coherent excitation applied between leads H and G [Fig. 1(d)]. The heating tone is generated by a room-temperature microwave generator and delivered to the sample through fifty-ohm coaxial transmission lines, a number of commercial attenuators and filters inside the cryostat, and finally a symmetrically coupled on-chip co-planar waveguide (CPW) resonator with a fundamental resonance frequency equal to the heater frequency. We calibrated the attenuation of the commercial components, assumed negligible attenuation for resonant transmission through the overcoupled CPW resonator,⁵⁵ and estimated $R_{N,\text{long}}$ based on resistivities of the dc coupled samples in order to take into account the small ($\sim 15\%$) amount of power reflected due to $R_{N,\text{long}} > 50 \Omega$. The CPW resonator is strongly coupled to the transmission lines, which leads to a low loaded quality factor of 10^2 compared to typical internal quality factors of 10^4 , hence justifying the full transmission assumption. The resonator acts as a Lorentzian bandpass filter that isolates the detector from non-thermal noise at other frequencies and reduces the electron-photon thermal conductance, which would otherwise be close to G_Q due to the intentional matching between the characteristic impedance of the heating line and the long junction. We note that similar band

or low pass filtering is in general practical in cQED where the thermal frequency $k_B T_b / \hbar$ is typically much smaller than the photon frequency of interest.

We probe the electron temperature through the reflection coefficient of a tank circuit that consists of on-chip parallel plate capacitors $C_1 \sim 100$ pF, C_2 , and C_g together with the mostly reactive admittance $Z(T_e)^{-1}$ of the short SNS junction [Fig. 1(d)]. For Sample R (F), $C_1 = 25C_2 = 75C_g$ ($C_1 = C_2 = 10C_g$). In the samples measured in rf mode, the short junction in fact consists of six SNS junctions made of alternating 150 – 200 nm pieces of superconductor and normal-metal, but they are treated as one effective admittance in this article. In linear response, the tank circuit in Sample R (F) is a harmonic oscillator with a resonance frequency $f_0 \approx 1/(2\pi\sqrt{LC})$ of 1.3 GHz (430 MHz) and quality factor of ten (hundred). Here $C^{-1} = C_1^{-1} + C_2^{-1}$ and $L = -1/(\omega \text{Im}\{Z(T_e)^{-1}\}) \sim 1$ nH is the effective junction inductance at angular frequency ω . The quality factor is governed by the external coupling capacitor C_g and internal losses within the resonator.^{53,56} As the junction heats up, $L \propto 1/I_c$ increases and hence f_0 decreases. We define f_0 as $A(T_e)$ in rf mode and extract it by measuring the reflection over a range of frequencies near f_0 . The measurement signal is generated and digitized at room temperature, but the sample is protected from high-temperature noise by a number of attenuators and amplifiers inside the cryostat. We separate the input and output of the reflection measurement with a resistive splitter and isolate the sample from amplifier noise with attenuators. These should be replaced by circulators in future bolometric applications requiring high signal-to-noise ratio.

As in dc mode, we assume that f_0 does not vary with T_b at constant T_e . In addition to the reasons discussed in the previous section, this assumption is justified by the nearly linear response of the SNS junction at low currents. Nonlinearities that couple incoherent fluctuations to the reflection measurement become important only when the current fluctuations become comparable to I_c , i.e., only on the energy scale of the Josephson energy $E_J > 2$ K. The nearly linear behavior together with the small heating currents ($\sqrt{P_{\text{local}}/R_{N,\text{long}}} \sim$ nA) also prevents cross-talk between the heating and thermometry signals, even in Sample F where $C_1 = C_2$.

III. DIFFERENTIAL THERMAL CONDUCTANCE

We define the differential thermal conductance between the nanowire electrons (e) and cryostat phonons (b) as the increase in the power flow between the two as T_b is decreased and T_e is kept constant, i.e.,

$$\tilde{G}_{e-b} = -\frac{\partial P_{e-b}(T_e, T_b)}{\partial T_b}, \quad (1)$$

where $P_{e-b} = (T_e - T_b)G_{e-b}$ is the net power flow from e to b and $G_{e-b}(T_e, T_b)$ is the non-differential thermal conductance [Fig. 1(a)]. Our definition is closely related to previous definitions of differential³⁸ or dynamic⁵⁷ thermal conductance, but with the roles of T_e and T_b exchanged. In steady state, the

temperatures satisfy the power balance equation

$$P_{\text{local}} + P_x(T_e, T_x) = P_{e-b}(T_e, T_b), \quad (2)$$

where a T_b -independent power P_x quantifies unintentional parasitic heating, which we represent as a weak coupling G_x to an independent temperature bath (T_x) in Fig. 1(a). The parasitic heating may be due to radiation leaking in from warmer parts of the cryostat or due to non-thermal noise from electronics. Because \tilde{G}_{e-b} is independent of this parasitic heating, we can compare it directly to the theoretical predictions for different channels, such as $\tilde{G}_{e-b} = \pi^2 k_b^2 T_b / 3h$ for matched single-channel conduction or $\tilde{G}_{e-b} = 5\Sigma V_0 T_b^4$ for electrons thermalized by bulk phonons in a metal of volume V_0 and coupling strength Σ . Note that T_e appears in these predictions only for non-linear channels that include cross terms of T_b and T_e in P_{e-b} . By measuring \tilde{G}_{e-b} , we can therefore experimentally investigate which thermalization channels dominate, even without a calibrated T_e sensor. Furthermore, \tilde{G}_{e-b} is the correct quantity for estimating the thermal-energy-fluctuation limited NEP due to coupling to T_b , which we consider to be of greater interest than fluctuations in the parasitic heating originating from imperfect shielding and filtering.

A. Isothermal technique and measured \tilde{G}_{e-b}

Our method of obtaining \tilde{G}_{e-b} is based on mapping contours of constant $A(T_e)$ in the (T_b, P_{local}) -plane. Specifically, $-\tilde{G}_{e-b}$ is given by the slope of a contour of $A(T_e)$ in the (T_b, P_{local}) -plane, as seen by differentiating Eq. (2) with respect to T_b while holding T_e constant. This is the same principle as in the so called isothermal technique used previously in TES-type samples,^{58–60} except that we take parasitic heating into account and therefore need to distinguish \tilde{G}_{e-b} from G_{e-b} even in the $P_{\text{local}} \rightarrow 0$ limit. Appendix A discusses some caveats of the isothermal technique that may arise if a more general thermal model than that of Fig. 1(a) is required to capture the physics of the system.

We apply this method to the measured typical switching currents shown in Figure 2(b) for Sample A. In order to draw smooth contours of $A(T_e)$, we fit a phenomenologically chosen smooth function $I_s^*(T_b, P_{\text{local}})$ to the data points; the details of the smoothing function do not affect the extracted \tilde{G}_{e-b} averaged over a T_b -scale larger than the data point spacing. We then compute $-\partial P_{\text{local}} / \partial T_b = \tilde{G}_{e-b}$ in the $P_{\text{local}} \rightarrow 0$ limit for many such contours and show the resulting curve in Fig. 3, along with the results from all other samples. The results are similar for gradients computed at non-zero P_{local} (not shown).

The temperature range in Fig. 3 is fundamentally limited at the high end by the breakdown of the assumption that the heating current is negligible compared to the thermometer current. At the low end, the vanishing magnitude of $\partial_{T_b} A(T_e(T_b, P_{\text{local}}, P_x))$ prevents extracting $-\partial P_{\text{local}} / \partial T_b$ mainly due to slow drifts in P_x on the time scale of several hours. In practice, a limited amount of data also restricts the T_b range of some of the curves, e.g., for Sample C.

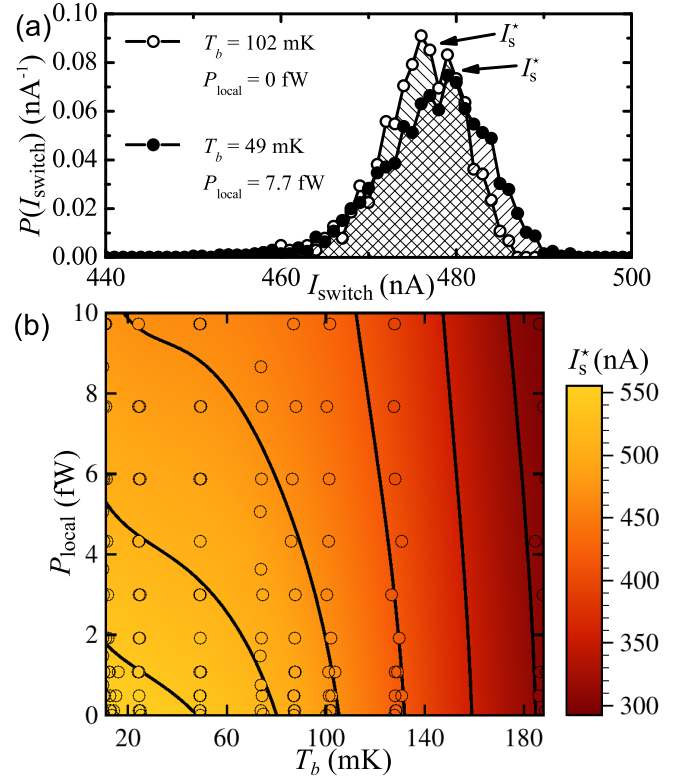


FIG. 2. (Color online) (a) Switching probability density as a function of current through the short SNS junction. The arrows indicate the extracted typical switching currents I_s^* . (b) Measured I_s^* (color inside circles) at different bath temperatures T_b and heating powers P_{local} . Black curves indicate contours of constant $A(T_e) = I_s^*$, as determined from a smoothing function (color outside circles). Both panels are for Sample A (see Table I).

B. Comparison to predicted mechanisms

We analyze Fig. 3 in terms of contributions arising from the nanowire electrons being coupled to substrate phonons,³⁵ photons in the electromagnetic environment,^{44,46} and quasiparticles in the superconductor leads.^{61,62} We do not expect a measurable contribution from phase slips in the leads.⁶³

Coupling of the nanowire electrons to substrate phonons is expected to contribute $5\Sigma V_0 T_b^4 = G_p$ to \tilde{G}_{e-b} , where $\Sigma \approx (3 \pm 1) \times 10^9 \text{ W/m}^3 \text{ K}^5$ for $\text{Au}_{.75}\text{Pd}_{.25}$ ^{64,65} and $V_0 = (100 \text{ nm})^3$ is a typical volume of our nanowires. This leads to the estimate $G_p = 2 \text{ fW/K}$ at $T_b = 100$ mK, which is one to two orders of magnitude less than the measured values. Furthermore, the observed scaling of \tilde{G}_{e-b} is much weaker than T_b^4 at the lowest temperatures (Fig. 3), suggesting that the phonon channel is insignificant for Samples B, C, R, and F. Above 80 mK, Samples A and N on the other hand approach the expected dependence for thermalization via phonons in a volume of roughly $130 \times (100 \text{ nm})^3$. This is similar to the measured volume of Sample N [$70 \times (100 \text{ nm})^3$] and can be explained for Sample A by an accidental galvanic contact between one of the Al leads and the tip of the corresponding normal-metal shadow [see Fig. 1(b)]. In that case, ther-

TABLE I. Parameters for the long and short sections [Fig. 1(b)] of the nanowire in each sample. Here, t is the nanowire thickness measured by a quartz crystal deposition monitor. We extracted lengths and widths from micrographs and measured the normal-state resistance R_N at $T_b = 10$ mK in dc mode. In rf mode, R_N is an estimate based on size and typical resistivity. We also provide the experimentally observed differential thermal conductance \tilde{G}_{e-b} at 70 mK bath temperature.

sample	t (nm)	Long section			Short section			$T_b = 70$ mK \tilde{G}_{e-b} (fW/K)
		length (nm)	width (nm)	R_N (Ω)	length (nm)	width (nm)	R_N (Ω)	
A	20	720	80	120	250	100	40	130
B	20	980	150	80	310	140	30	40
C	20	750	50	300	273	60	100	30
N(Nb)	60	1700	440	6.8	180	440	4.3	80
R	25	1400	140	100 (est.)	6×180	200		10
F	20	1400	130	130 (est.)	6×180	140		10

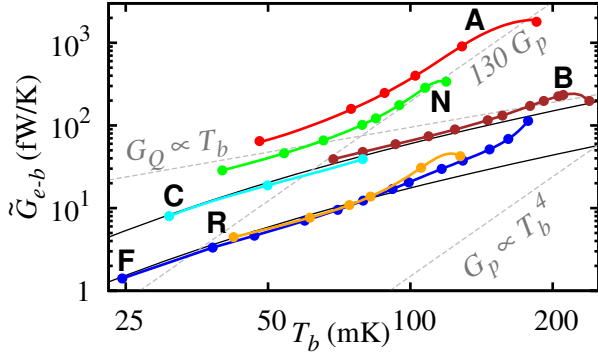


FIG. 3. (Color online) Differential thermal conductance $\tilde{G}_{e-b}(T_b)$ (solid curves with points) for dc samples (A, B, C, and N) and rf samples (R and F) against bath temperature T_b . Each point indicates the T_b value for a set of measured data [see Fig. 2(b)]. The dashed lines show the quantum of thermal conductance G_Q and the phonon contribution G_p for a typical nanowire volume of $(100 \text{ nm})^3$ and for a large volume of $130 \times (100 \text{ nm})^3$. Solid black curves correspond to the contribution of electron–photon coupling given a phenomenological model described in Appendix B and Fig. 5.

mal resistance over the short superconducting link between the nanowire and the shadow is negligible⁴⁸ and thermalization is limited by electron-phonon coupling in the combined nanowire–shadow volume of approximately $130 \times (100 \text{ nm})^3$, leading to results comparable to Courtois et al.⁵⁴

In the quasiparticle channel, electrons with energy higher than the superconductor energy gap Δ diffuse into the three superconductor leads.⁶² The thermal conductance for long superconductor leads is suppressed from the normal state value by a factor of $6(y^2 + 2y + 2)e^{-y}/\pi^2$ where $y = \Delta/(k_B T_{qp})$.^{48,49,66} At quasiparticle temperature $T_{qp} = 100$ mK this corresponds to only a few aW/K even for Al. However, the effective T_{qp} can be much higher than T_b ,^{61,67,68} so we chose to increase Δ in Sample N by using Nb instead of Al. Since at low temperatures \tilde{G}_{e-b} for Sample N is similar to the other dc mode samples (Fig. 3), we conclude that quasiparticles in the superconductor leads do not significantly add to the total heat conductance. This argument also applies to quasiparticles excited by multiple Andreev reflections.⁶⁹

Electron–photon coupling contributes a volume and material independent term to \tilde{G}_{e-b} , with a theoretical maximum value of $2G_Q \propto T_b$ which is reached when both junctions are perfectly matched to a resistive environment. In general, the matching varies as a function of frequency, causing deviations from the linear T_b dependence. We indeed observe a T_b dependence that falls between linear and quadratic in the low-temperature regime (except for Sample A). This is consistent with thermalization through poor but non-vanishing matching of the sample and environment impedances over a broad range of thermally excited frequencies. Furthermore, \tilde{G}_{e-b}/G_Q is notably smaller for rf samples (~ 0.1) than dc samples (~ 0.5) which differ essentially only in their coupling to the electromagnetic environment. Thus we attribute the observed low-temperature heat conductance to the photonic channel.

Since we did not intentionally engineer strong electromagnetic coupling to the sample, the exact physical structure constituting the dissipative environment remains unknown. Instead, in Appendix B we use a simple model of parasitic capacitive coupling to a resistive environment. This model reproduces the observed low-temperature thermal conductances shown in Fig. 3 with realistic values of the free parameters (see Fig. 5).

IV. CONCLUSION

We introduced a hot-electron nanobolometer integrated with a microwave transmission line input and a broad-band rf readout. We measured the differential thermal conductance for multiple samples in substantially different materials and electromagnetic environments and found values as low as 5 fW/K at 50 mK, attributed to parasitic electron–photon coupling. This value implies a fundamental thermal-energy-fluctuation limited noise level that is low enough for applications of great practical interest, in particular on-chip bolometric measurements in circuit quantum electrodynamics. Demonstrating such low noise-equivalent-powers in practice will require technical improvements in the amplification of the readout signal and possibly in sample shielding, if fluctuations in parasitic heating end up limiting performance. Finally, we introduced a precise definition of differential thermal conductance in the presence of a parasitic heating term, which

is non-negligible in many experiments at millikelvin temperatures.

ACKNOWLEDGMENTS

We thank Tero Heikkilä for helpful discussions and Leif Grönberg for depositing Nb thin films on some samples. We also gratefully acknowledge the provision of facilities and technical support by Aalto University at Micronova Nanofabrication Centre and the financial support from Emil Aaltonen Foundation, the European Research Council under Grant 278117 (“SINGLEOUT”), Academy of Finland under Grants 135794, 138903, 141015, 260880, 265675, 272806, and 251748 (“COMP”), the Finnish Cultural Foundation, and the European Metrology Research Programme (“EXL03 MICROPHOTON”). The EMRP is jointly funded by the EMRP participating countries within EURAMET and the European Union. We also thank all developers of the open-source lab environment QTLAB.

Appendix A: Extended thermal models

The main advantage of the isothermal technique is that it works in the presence of an unknown parasitic heating power without requiring calibration of the T_e sensor. However, the technique can lead to invalid conclusions if the thermal model shown in Fig. 1(a) does not accurately describe the system. Here we present two more detailed thermal models (see Fig. 4) that illustrate why the isothermal technique can in certain circumstances lead to underestimation of the thermal energy fluctuations and the associated NEP.

We first note that the technique gives the total thermal conductance of all the intermediate thermal links between the electron gas and the phonons of the cryostat baseplate. This leads to underestimation of T_e fluctuations if the bottleneck in heat conduction is G_{I-b} between a large intermediate thermal reservoir and the bath, rather than G_{e-I} between the electron gas and the intermediate reservoir [see Fig. 4(a)]. As argued in the main text, the normal metal shadow of one of the leads indeed constitutes such an intermediate reservoir for Sample A. However, in general it is unlikely that $G_{I-b} < G_{e-I} \ll G_Q$ for macroscopic intermediate reservoirs. On the other hand, mesoscopic bosonic reservoirs such as phonon⁷⁰ or photon modes tend to have negligible heat capacity compared to that of the electron gas. In that case the simpler model in Fig. 1(a) is appropriate for assessing T_e fluctuations, although G_{e-b} is determined by G_{I-b} .

We also consider adding an additional parasitic heating power to the intermediate reservoir [see Fig. 4(b)]. This model is more complex but potentially relevant at the lowest bath temperatures where the constant parasitic power $T_x G_{x-I}$ may not be negligible compared to $T_b G_{I-b}$, even if $G_{I-b} \gg G_{e-I}$. This scenario would be sufficient to prevent the intermediate temperature T_I from following T_b , leading to underestimation of the conductance between T_e and T_b . We do not have evidence that this phenomenon plays a noticeable role in

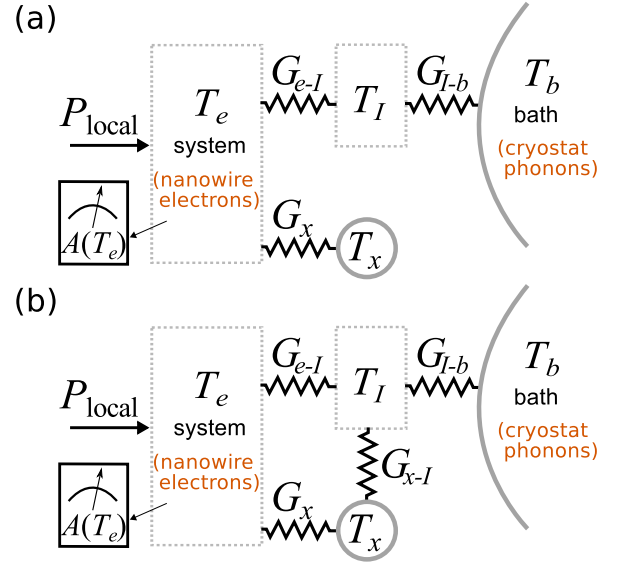


FIG. 4. (Color online) (a) Extended thermal model including an intermediate reservoir at temperature T_I coupled to the nanowire electrons by G_{e-I} and to the cryostat phonons by G_{I-b} . (b) Same model as in (a) but with an additional parasitic heating power $T_x G_{x-I}$ directly coupled to the intermediate reservoir. See the caption of Fig. 1(a) for definitions of other symbols.

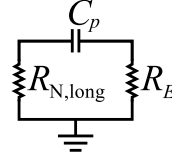


FIG. 5. Effective model for parasitic capacitive coupling C_p of the long junction ($R_{N,\text{long}}$) to a resistive environment (R_E). This model produces the upper (lower) black solid curve in Fig. 3 with $R_{N,\text{long}}$, R_E , and C_p equal to 130 Ω , 120 Ω , and 300 fF (130 Ω , 1.5 k Ω , and 45 fF), respectively.

our experiments, but ultimately such speculation can be conclusively dismissed only by direct measurement of the NEP.

Appendix B: Effective electromagnetic environment

Figure 5 shows a simple effective model for the parasitic electron–photon coupling between the detector and an unidentified electromagnetic environment. We approximate the detector impedance as $R_{N,\text{long}}$, although the real part of the short junction admittance can contribute at high frequencies. The capacitive coupling leads to better decoupling of the sample from the environment as the thermal frequency $k_B T_b / h$ decreases, leading to superlinear T_b dependence as observed in Fig. 3. We calculate the results numerically using formulas given by Pascal et al.⁴⁶

Although the values of the resistance of the environment R_E and the parasitic capacitance C_p have been chosen to fit the measured data, their magnitudes are reasonable (see

Fig. 5). In dc mode, the first well defined high impedance (1 k Ω) is centimeters away from the device on the printed circuit board, making stray capacitances in the pF range realistic, both between different signal lines and the signal lines and the metallic sample enclosure. In rf mode, 45 fF is similar to the

design value of the three-finger interdigitated coupling capacitor of the on-chip CPW resonator (see Göppl et al.⁵⁵) used as a band-pass filter for the heating tone. In both cases, the dissipation quantified by R_E^{-1} may arise from dielectric losses in the intentional or unintentional capacitors or from unintentionally generated shielding currents in normal metals.

-
- * joonas.govenius@aalto.fi
- ¹ B. Karasik, A. Sergeev, and D. Prober, *IEEE Trans. Terahertz Sci.* **1**, 97 (2011).
 - ² D. J. Benford and S. H. Moseley, *Nucl. Instrum. Methods Phys. Res., Sect. A* **520**, 379 (2004).
 - ³ A. Blais, R. S. Huang, A. Wallraff, S. M. Girvin, and R. J. Schoelkopf, *Phys. Rev. A* **69**, 062320 (2004).
 - ⁴ A. Wallraff, D. I. Schuster, A. Blais, L. Frunzio, R. S. Huang, J. Majer, S. Kumar, S. M. Girvin, and R. J. Schoelkopf, *Nature (London)* **431**, 162 (2004).
 - ⁵ D. Riste, M. Dukalski, C. A. Watson, G. de Lange, M. J. Tiggelman, Y. Blanter, K. W. Lehnert, R. N. Schouten, and L. DiCarlo, *Nature (London)* **502**, 350 (2013).
 - ⁶ P. D. Nation, J. R. Johansson, M. P. Blencowe, and F. Nori, *Rev. Mod. Phys.* **84**, 1 (2012).
 - ⁷ C. K. Hong, Z. Y. Ou, and L. Mandel, *Phys. Rev. Lett.* **59**, 2044 (1987).
 - ⁸ E. Knill, R. Laflamme, and G. J. Milburn, *Nature (London)* **409**, 46 (2001).
 - ⁹ M. P. da Silva, D. Bozyigit, A. Wallraff, and A. Blais, *Phys. Rev. A* **82**, 043804 (2010).
 - ¹⁰ C. Lang, C. Eichler, L. Steffen, J. M. Fink, M. J. Woolley, A. Blais, and A. Wallraff, *Nature Phys.* **9**, 345 (2013).
 - ¹¹ J. Wei, D. Olaya, B. S. Karasik, S. V. Pereverzev, A. V. Sergeev, and M. E. Gershenson, *Nature Nano.* **3**, 496 (2008).
 - ¹² B. S. Karasik and R. Cantor, *Appl. Phys. Lett.* **98**, 193503 (2011).
 - ¹³ M. Kenyon, P. K. Day, C. M. Bradford, J. J. Bock, and H. G. Leduc, *Proc. SPIE* **6275**, 627508 (2006).
 - ¹⁴ D. F. Santavica, B. Reulet, B. S. Karasik, S. V. Pereverzev, D. Olaya, M. E. Gershenson, L. Frunzio, and D. E. Prober, *Appl. Phys. Lett.* **96**, 083505 (2010).
 - ¹⁵ B. S. Karasik, S. V. Pereverzev, A. Soibel, D. F. Santavica, D. E. Prober, D. Olaya, and M. E. Gershenson, *Appl. Phys. Lett.* **101**, 052601 (2012).
 - ¹⁶ P. K. Day, H. G. Leduc, B. A. Mazin, A. Vayonakis, and J. Zmuidzinas, *Nature (London)* **425**, 817 (2003).
 - ¹⁷ R. M. J. Janssen, J. J. A. Baselmans, A. Endo, L. Ferrari, S. J. C. Yates, A. M. Baryshev, and T. M. Klapwijk, *Appl. Phys. Lett.* **103**, 203503 (2013).
 - ¹⁸ P. J. de Visser, J. J. A. Baselmans, J. Bueno, N. Llombart, and T. M. Klapwijk, *Nature Commun.* **5**, 3130 (2014).
 - ¹⁹ M. Nahum and J. Martinis, *Physica B* **194**, 109 (1994).
 - ²⁰ D. R. Schmidt, C. S. Yung, and A. N. Cleland, *Appl. Phys. Lett.* **83**, 1002 (2003).
 - ²¹ D. R. Schmidt, K. W. Lehnert, A. M. Clark, W. D. Duncan, K. D. Irwin, N. Miller, and J. N. Ullom, *Appl. Phys. Lett.* **86**, 053505 (2005).
 - ²² D. E. Prober, J. D. Teufel, C. M. Wilson, L. Frunzio, M. Shen, R. J. Schoelkopf, T. R. Stevenson, and E. J. Wollack, *IEEE Trans. Appl. Supercond.* **17**, 241 (2007).
 - ²³ S. Komiyama, O. Astafiev, V. Antonov, T. Kutsuwa, and H. Hirai, *Nature (London)* **403**, 405 (2000).
 - ²⁴ H. Hashiba, V. Antonov, L. Kulik, A. Tzalenchuk, and S. Komiyama, *Nanotechnol.* **21**, 165203 (2010).
 - ²⁵ S. Komiyama, *IEEE J. Sel. Top. Quant. Electr.* **17**, 54 (2011).
 - ²⁶ K. C. Fong and K. C. Schwab, *Phys. Rev. X* **2**, 031006 (2012).
 - ²⁷ J. Yan, M.-H. Kim, J. A. Elle, A. B. Sushkov, G. S. Jenkins, H. M. Milchberg, M. S. Fuhrer, and H. D. Drew, *Nature Nano.* **7**, 472 (2012).
 - ²⁸ M. Mittendorff, S. Winnerl, J. Kamann, J. Eroms, D. Weiss, H. Schneider, and M. Helm, *Appl. Phys. Lett.* **103**, 021113 (2013).
 - ²⁹ C. B. McKitterick, D. E. Prober, and B. S. Karasik, *J. Appl. Phys.* **113**, 044512 (2013).
 - ³⁰ Y. Kawano, T. Uchida, and K. Ishibashi, *Appl. Phys. Lett.* **95**, 083123 (2009).
 - ³¹ P. L. Richards, T. M. Shen, R. E. Harris, and F. L. Lloyd, *Appl. Phys. Lett.* **36**, 480 (1980).
 - ³² J. Bueno, M. D. Shaw, P. K. Day, and P. M. Echternach, *Appl. Phys. Lett.* **96**, 103503 (2010).
 - ³³ P. M. Echternach, K. J. Stone, C. M. Bradford, P. K. Day, D. W. Wilson, K. G. Megerian, N. Llombart, and J. Bueno, *Appl. Phys. Lett.* **103**, 053510 (2013).
 - ³⁴ J. E. Sadleir, S. J. Smith, S. R. Bandler, J. A. Chervenak, and J. R. Clem, *Phys. Rev. Lett.* **104**, 047003 (2010).
 - ³⁵ F. C. Wellstood, C. Urbina, and J. Clarke, *Phys. Rev. B* **49**, 5942 (1994).
 - ³⁶ F. Giazotto, T. T. Heikkilä, G. P. Pepe, P. Heliö, A. Luukanen, and J. P. Pekola, *Appl. Phys. Lett.* **92**, 162507 (2008).
 - ³⁷ J. Voutilainen, M. A. Laakso, and T. T. Heikkilä, *J. Appl. Phys.* **107**, 064508 (2010).
 - ³⁸ J. C. Mather, *Appl. Opt.* **21**, 1125 (1982).
 - ³⁹ S. H. Moseley, J. C. Mather, and D. McCammon, *J. Appl. Phys.* **56**, 1257 (1984).
 - ⁴⁰ N. E. Booth, B. Cabrera, and E. Fiorini, *Annu. Rev. Nucl. Part. Sci.* **46**, 471 (1996).
 - ⁴¹ J. B. Pendry, *J. Phys. A* **16**, 2161 (1983).
 - ⁴² K. Schwab, E. A. Henriksen, J. M. Worlock, and M. L. Roukes, *Nature (London)* **404**, 974 (2000).
 - ⁴³ D. R. Schmidt, R. J. Schoelkopf, and A. N. Cleland, *Phys. Rev. Lett.* **93**, 045901 (2004).
 - ⁴⁴ M. Meschke, W. Guichard, and J. P. Pekola, *Nature (London)* **444**, 187 (2006).
 - ⁴⁵ S. Jezouin, F. D. Parmentier, A. Anthore, U. Gennser, A. Cavanna, Y. Jin, and F. Pierre, *Science* **342**, 601 (2013).
 - ⁴⁶ L. M. A. Pascal, H. Courtois, and F. W. J. Hekking, *Phys. Rev. B* **83**, 125113 (2011).
 - ⁴⁷ H. Okamoto and T. B. Massalski, *Bull. All. Ph. Diagr.* **6**, 229 (1985).
 - ⁴⁸ J. T. Peltonen, P. Virtanen, M. Meschke, J. V. Koski, T. T. Heikkilä, and J. P. Pekola, *Phys. Rev. Lett.* **105**, 097004 (2010).
 - ⁴⁹ E. V. Bezuglyi and V. Vinokur, *Phys. Rev. Lett.* **91**, 137002 (2003).
 - ⁵⁰ P. Dubos, H. Courtois, B. Pannetier, F. K. Wilhelm, A. D. Zaikin, and G. Schön, *Phys. Rev. B* **63**, 064502 (2001).
 - ⁵¹ F. Giazotto, T. T. Heikkilä, A. Luukanen, A. M. Savin, and J. P. Pekola, *Rev. Mod. Phys.* **78**, 217 (2006).

- ⁵² M. Meschke, J. T. Peltonen, H. Courtois, and J. P. Pekola, *J. Low Temp. Phys.* **154**, 190 (2009).
- ⁵³ P. Virtanen, F. S. Bergeret, J. C. Cuevas, and T. T. Heikkilä, *Phys. Rev. B* **83**, 144514 (2011).
- ⁵⁴ H. Courtois, M. Meschke, J. T. Peltonen, and J. P. Pekola, *Phys. Rev. Lett.* **101**, 067002 (2008).
- ⁵⁵ M. Göppl, A. Fagner, M. Baur, R. Bianchetti, S. Filipp, J. M. Fink, P. J. Leek, G. Puebla, L. Steffen, and A. Wallraff, *J. Appl. Phys.* **104**, 113904 (2008).
- ⁵⁶ B. Dassonneville, M. Ferrier, S. Guéron, and H. Bouchiat, *Phys. Rev. Lett.* **110**, 217001 (2013).
- ⁵⁷ P. L. Richards, *J. Appl. Phys.* **76**, 1 (1994).
- ⁵⁸ E. M. Gershenzon, G. N. Goltsman, A. I. Elantev, B. S. Karasik, and S. E. Potoskuev, *Sov. J. Low Temp. Phys.* **14**, 753 (1988).
- ⁵⁹ A. I. Elantev and B. S. Karasik, *Sov. J. Low Temp. Phys.* **15**, 379 (1989).
- ⁶⁰ B. S. Karasik, S. V. Pereverzev, D. Olaya, J. Wei, M. E. Gershenzon, and A. V. Sergeev, *IEEE Trans. Appl. Supercond.* **19**, 532 (2009).
- ⁶¹ J. T. Muhonen, M. Meschke, and J. P. Pekola, *Rep. Prog. Phys.* **75**, 046501 (2012).
- ⁶² V. Chandrasekhar, *Supercond. Sci. Technol.* **22**, 083001 (2009).
- ⁶³ K. Y. Arutyunov, D. S. Golubev, and A. D. Zaikin, *Phys. Rep.* **464**, 1 (2008).
- ⁶⁴ A. V. Timofeev, M. Helle, M. Meschke, M. Möttönen, and J. P. Pekola, *Phys. Rev. Lett.* **102**, 200801 (2009).
- ⁶⁵ J. T. Muhonen, A. O. Niskanen, M. Meschke, Yu, J. S. Tsai, L. Sainiemi, S. Franssila, and J. P. Pekola, *Appl. Phys. Lett.* **94**, 073101 (2009).
- ⁶⁶ J. Bardeen, G. Rickayzen, and L. Tewordt, *Phys. Rev.* **113**, 982 (1959).
- ⁶⁷ J. Aumentado, M. W. Keller, J. M. Martinis, and M. H. Devoret, *Phys. Rev. Lett.* **92**, 066802 (2004).
- ⁶⁸ P. J. de Visser, J. J. A. Baselmans, P. Diener, S. J. C. Yates, A. Endo, and T. M. Klapwijk, *Phys. Rev. Lett.* **106**, 167004 (2011).
- ⁶⁹ E. V. Bezuglyi, E. N. Bratus', V. S. Shumeiko, and G. Wendin, *Phys. Rev. B* **63**, 100501 (2001).
- ⁷⁰ L. M. A. Pascal, A. Fay, C. B. Winkelmann, and H. Courtois, *Phys. Rev. B* **88**, 100502 (2013).